

Research Paper

Enhanced Blood Suspensibility and Laser-Activated Tumor-specific Drug Release of Theranostic Mesoporous Silica Nanoparticles by Functionalizing with Erythrocyte Membranes

Jinghan Su^{1,2}, Huiping Sun^{1,3}, Qingshuo Meng^{1,2}, Pengcheng Zhang¹, Qi Yin¹, Yaping Li^{1,2}✉

1. State Key Laboratory of Drug Research & Center of Pharmaceutics, Shanghai Institute of Materia Medica, Chinese Academy of Sciences, 501 Haik Road, Shanghai 201203, China;
2. University of Chinese Academy of Sciences, Beijing 100049, China;
3. School of Pharmacy, Shenyang Pharmaceutical University, Shenyang, 110016, China.

✉ Corresponding author: Prof. Yaping Li, State Key Laboratory of Drug Research & Center of Pharmaceutics, Shanghai Institute of Materia Medica, Chinese Academy of Sciences, 501 Haik Road, Shanghai 201203, China. Email: ypLi@simm.ac.cn; Tel/Fax: +86-21-20231979.

© Ivyspring International Publisher. This is an open access article distributed under the terms of the Creative Commons Attribution (CC BY-NC) license (<https://creativecommons.org/licenses/by-nc/4.0/>). See <http://ivyspring.com/terms> for full terms and conditions.

Received: 2016.08.18; Accepted: 2016.10.11; Published: 2017.01.07

Abstract

Mesoporous silica nanoparticles (MSNs), with their large surface area and tunable pore sizes, have been widely applied for anticancer therapeutic cargos delivery with a high loading capacity. However, easy aggregation in saline buffers and limited blood circulation lifetime hinder their delivery efficiency and the anticancer efficacy. Here, new multifunctional MSNs-supported red-blood-cell (RBC)-mimetic theranostic nanoparticles with long blood circulation, deep-red light-activated tumor imaging and drug release were reported. High loading capacities were achieved by camouflaging MSNs with RBC membrane to co-load an anticancer drug doxorubicin (Dox) (39.1 wt%) and a near-infrared photosensitizer chlorin e6 (Ce6) (21.1 wt%). The RBC membrane-coating protected drugs from leakage, and greatly improved the colloidal stability of MSNs, with negligible particle size change over two weeks. Upon an external laser stimuli, the RBC membrane could be destroyed, resulting in 10 times enhancement of Dox release. In a 4T1 breast cancer mouse model, the RBC-mimetic MSNs could realize *in vivo* tumor imaging with elongated tumor accumulation lifetime for over 24 h, and laser-activated tumor-specific Dox accumulation. The RBC-mimetic MSNs could integrate the Ce6-based photodynamic therapy and Dox-based chemotherapy, completely suppress the primary tumor growth and inhibit metastasis of breast cancer, which could provide a new strategy for optimization of MSNs and efficient anticancer drug delivery.

Key words: Mesoporous silica nanoparticles, RBC-mimetic, Drug release, Fluorescence imaging, Metastasis.

Introduction

Breast cancer is a serious hazard to woman health. Current single therapeutic effect remains unsatisfying, especially for high metastatic breast cancer, which lead to over 90% of death [1]. Up to now, no effective treatment or strategy has been approved by Food and Drug Administration (FDA). Theranostic nanomedicines could integrate multiple pathways of cancer diagnosis and treatment with

many advantages, *e.g.* synergetic efficacy, minimized side effects and reversal of drug resistance, which showed enormous potentials for efficient anticancer therapy[2-4].

To maximize the cooperative effect, different amount of therapeutic agents should be delivered to the same tumor cells with sufficient dose. Mesoporous silica nanoparticles (MSNs) showed the great

potential for drug delivery based on their attractive features, such as controllable size, large surface area ($>1000 \text{ m}^2 \text{ g}^{-1}$), tunable pore sizes (2-20 nm) and high pore volume [5]. The major advantage is that the pore size and surface chemistries can be easily modified to accommodate a variety of components (chemotherapeutic drugs, RNA, peptides or photosensitizers, etc) with high loading capacities [6]. However, there are still some limitations for efficient drug delivery. One is the dispersion of MSNs. Since MSNs are generally charge-stabilized, they may be destabilized to form aggregation in saline buffers such as blood, which leads to the leakage and premature release of the physically adsorbed drugs [7]. Another is the limited circulation lifetime caused by the recognition by the reticulo endothelial system (RES), which could result in sublethal tumor-targeted distribution of therapeutic drugs [8, 9]. The great efforts have been made to modify MSNs with various polymers, such as polyethylene glycol [10], block copolymers [11], chitosan [12]), and bulky groups [13] (e.g. Au, CdS nanocrystals) through chemical modification or electrostatic action, which could stabilize MSNs, prolong the blood circulation and control the release of drugs [14]. However, the functionalization could reduce the surface area and pore size, limiting the following drug loading. While drug was pre-loaded, it could bring about an inevitable drug loss during the long time chemical modification and the repetitive purify of MSNs [15]. To enhance the tumor accumulation of MSNs, their surfaces were often modified with tumor-specific ligands to activate tumor targeting. However, the *in vivo* biodistribution of many ligand-modified nanoparticles is not satisfied as initially expected because the ligand attachment often decreases the ligand affinity to receptors on tumor cells and their circulation lifetime [16]. Therefore, it is very urgent to find a simple and efficient strategy to overcome these deficiencies to achieve efficient tumor drug delivery.

Remarkable biocompatibility, immune-invasive capacity and protecting cargoes for long circulation lifetime, all these requirements inspired us to associate the natural long circulating carrier, red blood cells (RBCs), for efficient drug delivery [17-19]. It is reported that the abundant glycans, proteins and receptors on the RBC membranes' surfaces play an indispensable role for avoiding the immune system attack of RBCs [20]. The intact RBC membrane could directly coat on the nanoparticles' surface to inherit the functions of RBCs [21] and has exhibited many advantage functions [22, 23]. Besides, utilizing a well-established top-down method, this membrane coating could be oriented-right [24-26], and avoid complex chemical modification, which may interfere

with the loading capacity of MSNs. External stimuli, such as light [27], ultrasound [28], and magnetic field [29], have been widely used to activate tumor targeting. Among them, utilizing an external laser to realize controllable drug release, has received more attention, which is noninvasive, deep tumor penetration and could be controlled remotely and precisely [30].

Herein, we designed a laser-responsive MSNs-supported RBC-mimetic nano drug delivery system (NDDS) with enhanced blood circulation and tumor-specific drug release. A photosensitizer chlorin e6 (Ce6) and doxorubicin (Dox) were co-loaded in the porous of stellate MSNs (MSNs-Dox/Ce6), and RBC-mimetic vesicles (RVs) extracted from RBC membrane were coated on the MSNs surface to form the final RVs-coated MSNs-Dox/Ce6 (RMSNs-Dox/Ce6) (Scheme 1). We hypothesize the RBC membrane could stabilize MSNs in blood, protect the encapsulated drugs from leakage and enhance the circulating lifetime. In return, MSNs could suppress RBC membrane fluctuations and possess a high drug loading capacity. Owing to the fluorescence of Ce6, RMSNs-Dox/Ce6 could serve as an *in vivo* tumor imaging probe. Besides, when stimulated by an external laser, Ce6 could generate reactive oxygen species (ROS) and destroy the RBC membrane, as well as the tumor cell membrane, leading to a rapid Dox release and a tumor-specific Dox accumulation. We expected that RBC-mimetic MSNs could integrate the Ce6-based photodynamic therapy and the Dox-based chemotherapy to completely suppress the metastatic breast cancer.

Results and discussions

Preparation and characterization of RMSNs-Dox/Ce6

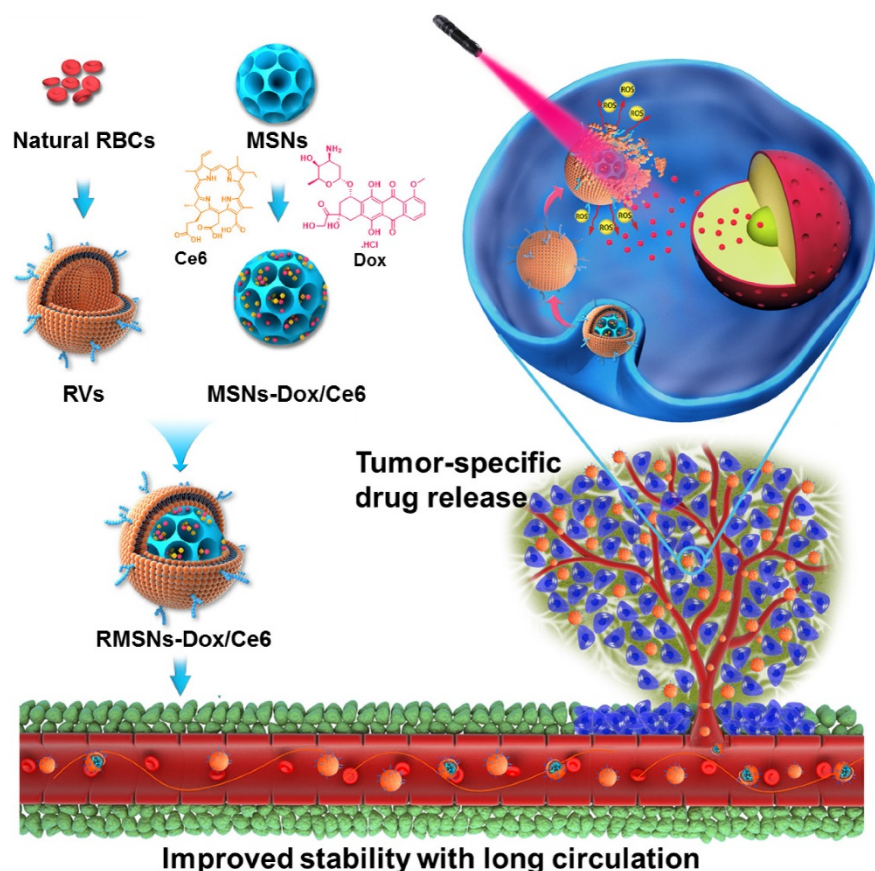
As illustrated in Scheme 1, we extracted RBC membrane vesicles (RVs) from RBCs, prepared Dox and Ce6 co-loaded MSNs (MSNs-Dox/Ce6), and then coated MSNs-Dox/Ce6 with RVs to fabricate the RVs-coated MSN-Dox/Ce6 (RMSNs-Dox/Ce6). In this work, stellate MSNs with a special radial pore morphology were chosen, which were recently reported as ideal scaffolds for medical applications and mass drug delivery [31-33]. The provided MSNs have the Brunauer-Emmett-Teller surface area of more than $1000 \text{ m}^2/\text{g}$, the well-defined conical pore size of 2.9 nm and the inter particle void size up to 50 nm. As shown in Figure 1A, the MSNs-Dox/Ce6 exhibited stellate morphology, while RMSNs-Dox/Ce6 were regular sphere with a core-shell structure. The high magnification of RMSNs-Dox/Ce6 transmission electron microscope

(TEM) images indicated the existence of the RBC membrane shell. The hydrodynamic diameter of the monodisperse mesoporous silica nanosphere was 91.2 nm (PDI= 0.108) (Figure 1B), and the zeta potential was determined to be +5.1 mV, which could be due to the potentially residual hexadecyl trimethyl ammonium Bromide (CTAB). The drug loading ratio (DL%) and encapsulation efficiency (EE%) were 39.8% and 97.6% for Dox, and those of Ce6 were 21.1% and 96.3%, respectively. The high loading capacities could be due to the high surface-volume ratio of MSNs. After RBC membrane coating, the particle size of MSNs-Dox/Ce6 increased to 107.7 nm (PDI= 0.121) with zeta potential decreasing to -14.0 mV, comparable to that of RVs (-15.0 mV), both suggested the successful coating of RVs onto the surfaces of MSNs.

An ideal nano-sized drug delivery system should keep its stability in blood circulation and controllably release drug in the tumor environment. Thus, the serum stability assay of MSNs-Dox/Ce6 and RMSNs-Dox/Ce6 was evaluated in 1640 medium

containing 10% FBS. The particle size of the MSNs significantly increased over time, indicating the unstable aggregation, while there was only slight size change of RVs-coated MSNs (RMSNs) throughout a long period time of two weeks (Figure S1). The aggregation phenomenon was also observed with the apparent precipitation in the bottom of the cube containing MSNs-Dox/Ce6 solutions, while the RMSNs-Dox/Ce6 sample maintained clear after two weeks' storage (Figure 1C). The stabilizing effect of RBC membrane could be attributed to the copious surface glycans, which are highly hydrophilic and supporting steric stabilization of cells [34].

Then we wonder whether the abundant proteins and receptors could play their role to evade immune attack. A western-blotting analysis confirmed that most of the membrane proteins were retained during the preparation of RV and RMSNs (Figure S2A). More importantly, CD47, the "don't eat me" biomarker of RBCs to prevent RES recognition, was confirmed on RMSNs' surfaces. Then we investigated the orientation of coated RBC membrane, and the bioactivity of these proteins on their surface, especially the function to escape the uptake by macrophage cells (Figure S2B-C). RBC membrane-coated MSNs showed significantly reduced internalization in mouse macrophage RAW 264.7 cells, with a 68.0% reduction of fluorescence intensity in cells. To identify the role of RBC membrane on the suppression of macrophage phagocytosis, synthesized lipid-coating MSNs (LMSNs) were used as an analog of RMSNs. The fluorescence image and the quantitative results indicated that the cellular uptake of MSNs was not reduced by lipid coating, confirming the right-side orientation of the coated RBC membrane, as well as the superior function of RBC membrane to artificial lipid membrane, with proteins on the surface for reducing the cellular uptake of MSNs by macrophage cells.



Scheme 1. The laser-responsive RBC-mimetic MSNs with long circulation lifetime and tumor-specific drug release for anti-metastasis breast cancer. The RBC membrane coated on the surface of MSNs could stabilize MSNs and prevent drugs from leakage. At the tumor lesion, the ROS generation under the laser stimuli could destroy the RBC membrane, resulting in an efficient drug distribution in the tumor cells.

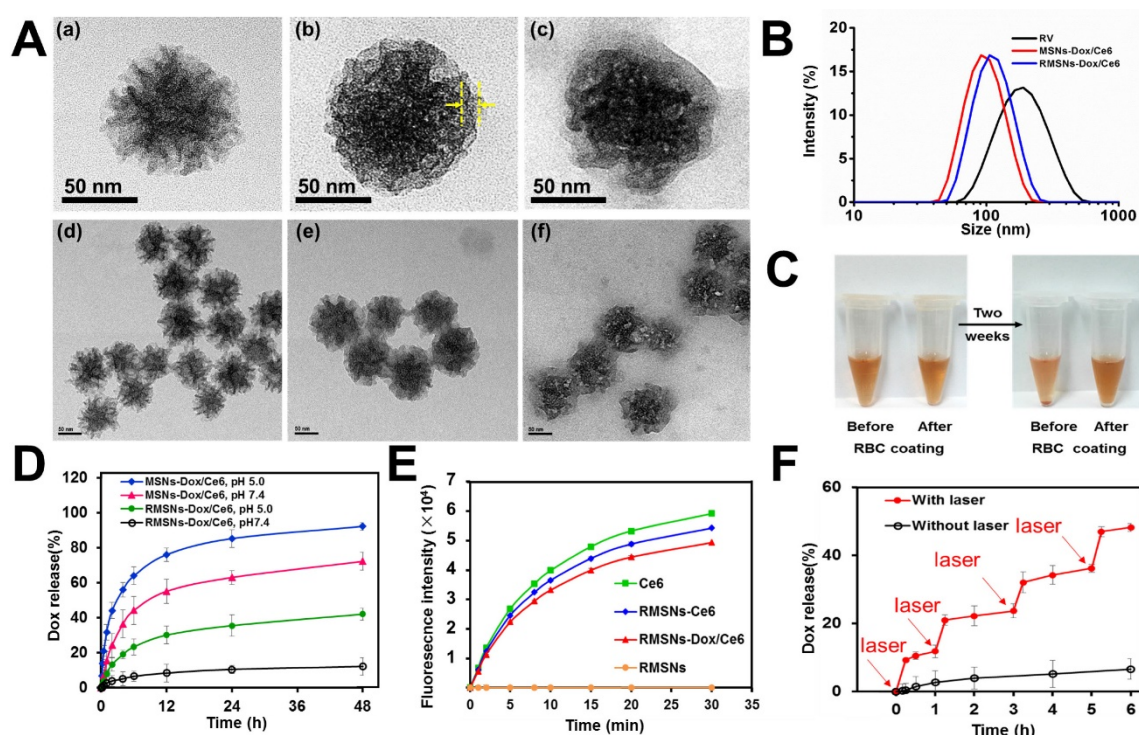


Figure 1. Characterization of RBC-mimetic MSNs. (A) Representative TEM images of (a), (d): MSNs-Dox/Ce6; (b), (e): RMSNs-Dox/Ce6, (c), (f): RMSNs-Dox/Ce6 irradiated by a 655nm laser at a laser power of 2 W cm^{-2} for 5 min. The yellow arrows indicated the RBC membrane coating. (B) Particle size distribution of RV, MSNs-Dox/Ce6 and RMSNs-Dox/Ce6. (C-D) Aggregation phenomena of MSNs in 1640 medium containing 10% FBS. (E) *In vitro* Dox release behavior from MSNs and RMSNs in PBS of different pH values at 37°C . (F) The increase of SOSG fluorescence as a result of ROS generation of free Ce6, Ce6-loaded RMSNs-Ce6, RMSNs-Dox/Ce6 and blank RMSNs under 655 nm laser irradiation at 2 W cm^{-2} . (G) *In vitro* Dox release profile at 37°C from RMSNs-Dox/Ce6 with or without laser irradiation. Red arrows indicated the time points of laser irradiation.

Then the *in vitro* Dox release behaviors of nanoparticles in different pH at 37°C were also investigated (Figure 1D). MSNs-Dox/Ce6 showed a fast Dox release profile in PBS (pH=7.4), with 55.2% cumulative release within 12 h and 72.3% after 48 h, which indicated the instability of MSNs-Dox/Ce6 in physical medium. After RVs coating, RMSNs-Dox/Ce6 showed a good stability with negligible drug release over 48 h. In addition, RMSNs-Dox/Ce6 and MSNs-Dox/Ce6 showed a pH-dependent release behavior with more Dox released at lower pH (pH= 5.0), which could be due to the more protonated silanols on the MSN surfaces when exposed to lower pH, leading to a decreased electrostatic interaction and dissociation of Dox from the MSN cores [35].

Ce6 was a widely-used photosensitizer for PDT with the fluorescence emission in the deep-red light region [36]. The fluorescence efficiency of Ce6 was evaluated by the UV-Vis spectroscopic measurement. As shown in Figure S3, free Ce6 displayed a maximum absorbance peak at 405 nm and an obvious signal at 650 nm. Successful Ce6 loading in MSNs was convinced with the identified characteristic absorption peak. The MSNs-Dox/Ce6 and RMSNs-Dox/Ce6 showed a slight red shift of Ce6's maximum peak compared to MSNs-Ce6, which was

probably due to the variations of the local refractive index of the surfacing medium [37]. The UV-Vis absorption of Dox was also recorded. Free Dox showed a wide maximum absorbance peak around 479 nm. After loading into MSN nanoparticles, the fluorescence signal of Dox was significantly decreased, which could be due to the high Dox concentration within MSNs-Dox/Ce6, resulting in self-quenching of fluorescence [38].

As generation of cytotoxic ROS is critical for photodynamic therapy of cancer, we evaluated the generation of singlet oxygen by RMSNs-Ce6 under the 655nm laser irradiation using singlet oxygen sensor green (SOSG) as a ROS probe. As shown in Figure 1E, blank RMSNs produced negligible ROS, while 655 nm laser-irradiated RMSNs-Dox/Ce6 produced significantly increased ROS over time within 30 min, which was similar to free Ce6 and RMSNs-Ce6. Besides, the production of ROS from 655 nm laser-irradiated RMSNs-Dox/Ce6 (Ce6 concentration = 10 ng/mL) was found to be positively correlated with the power density (Figure S4). The effective ROS generation of Ce6 in RMSNs-Dox/Ce6 enabled effective PDT treatment of breast cancer, and also suggested the potential for laser irradiation-triggered drug release.

We further evaluated the Dox release from

RMSNs-Dox/Ce6 triggered by laser irradiation (Figure 1F). After irradiated by a 655nm laser at 2 W cm⁻² for 5 min, Dox release from RMSNs-Dox/Ce6 surged from 0.5% to 10.6% at the starting point. Laser-triggered Dox release was also observed at 1 h, 3 h and 5 h, in which Dox was released from 2.7% to 21.0%, 4.3% to 32.1% and 5.8% to 46.9%, respectively. These results indicated that the release of Dox from RMSNs-Dox/Ce6 could be controlled by laser efficiently.

To investigate the effect of laser irradiation on Dox release, the final fluorescence of Dox in RMSNs-Dox/Ce6 was visualized by an image lab system (Figure S5). The fluorescence signal of Dox almost silenced in RMSNs-Dox/Ce6, it was probably due to the self-quenching of Dox fluorescence. Driven by the laser illumination, Dox was released and led to a significantly enhancement of Dox fluorescence. The mechanism could be that the laser-triggered ROS generation by Ce6 in RMSNs-Dox/Ce6 could disturb the permeability of cell membrane [39], and the loaded Dox was rapidly released. On the other hand, the fluorescence signal of Ce6 in the free Ce6 and RMSNs-Dox/Ce6 groups were significantly decreased after long-time laser irradiation (Figure S6), which was probably due to the photobleaching [40]. These results indicated that the RBC membrane coating could hinder the drug leakage from the cores on the MSNs' surface and promise a steady drug delivery, and the RMSNs-Dox/Ce6 could provide a

controllable drug release triggered by laser irradiation, leading to a promised and effective chemotherapy.

Laser-triggered activation of RMSNs-Dox/Ce6 *in vitro*

To further investigate the cellular uptake of Dox and laser-triggered Dox distribution of RMSNs-Dox/Ce6 in 4T1 breast cancer cells, the intracellular photoactivity of Ce6 in RMSNs-Dox/Ce6 was examined. 2',7'-dichlorofluorescein-diacetate (DCFH-DA) was used as a fluorescence probe of ROS (Figure 2A). Without laser illumination, non DCF signals were observed in free Dox, MSNs-Dox/Ce6 and RMSNs-Dox/Ce6 treated 4T1 cells, and the red fluorescence signals were mainly found surrounding the nuclei, respectively. After laser illumination with a 655nm laser for 5 min, the strong green fluorescence was observed in RMSNs-Dox/Ce6-treated cells, demonstrating the obvious generation of ROS and the cytosol diffusion of Ce6. Also observed was strong red fluorescence spots in the cytoplasm as well as the nuclei, which demonstrated that the laser-driven ROS generation could stimulate drug release and cytosol diffusion of Dox. The influence of laser power on intracellular ROS generation of RMSNs-Dox/Ce6 was further quantified by flow cytometry (Figure 2B). Since tumor cells treated with laser irradiation alone did not generate ROS (Figure S7), the intracellular ROS concentration was positively correlated with the power density, and reached to the peak value at a laser power of 2.5 W/cm².

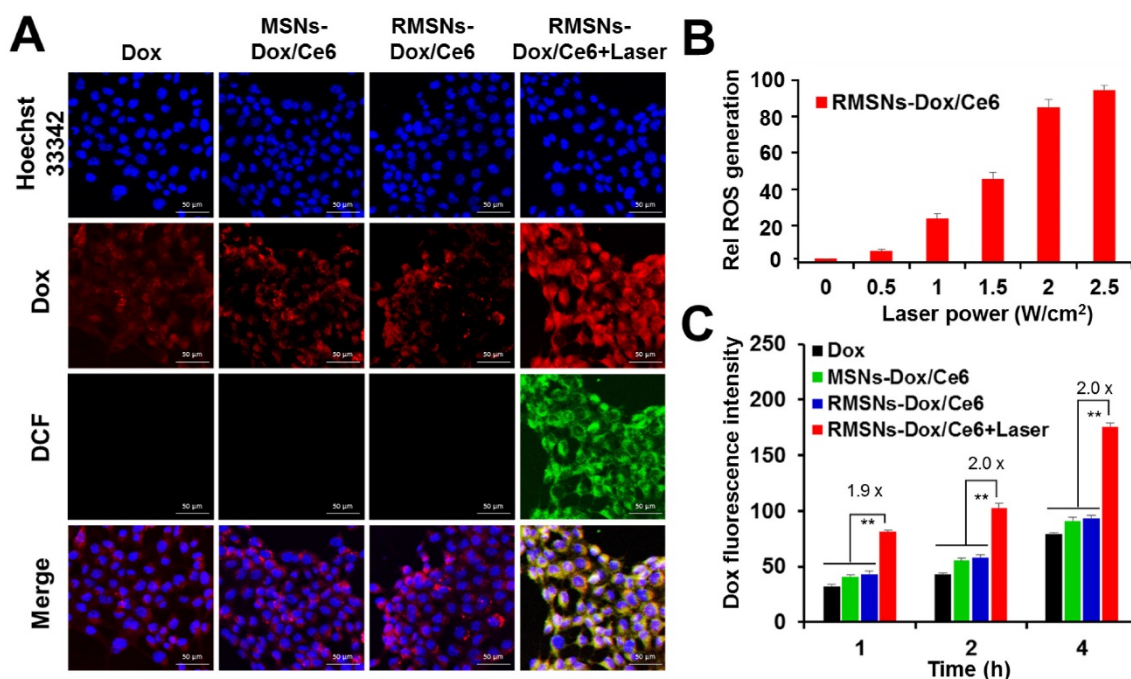


Figure 2. *In vitro* cellular uptake and ROS generation of RMSNs-Dox/Ce6. (A) Representative fluorescence images of 4T1 cells pre-incubated in free Dox, MSNs-Dox/Ce6, RMSNs-Dox/Ce6 and RMSNs-Dox/Ce6 with laser irradiation for 4 h, respectively. DCF was used as a probe for intracellular ROS generation. (nucleus: blue; Dox: red; DCF: green) Scale bar = 50 μ m. (B) Flow cytometric examination of intracellular ROS generation of RMSNs-Dox/Ce6 at different laser powers. (C) Quantitative analysis of Dox accumulation in 4T1 cells. Data were presented as mean \pm SD (n = 3), **P < 0.01.

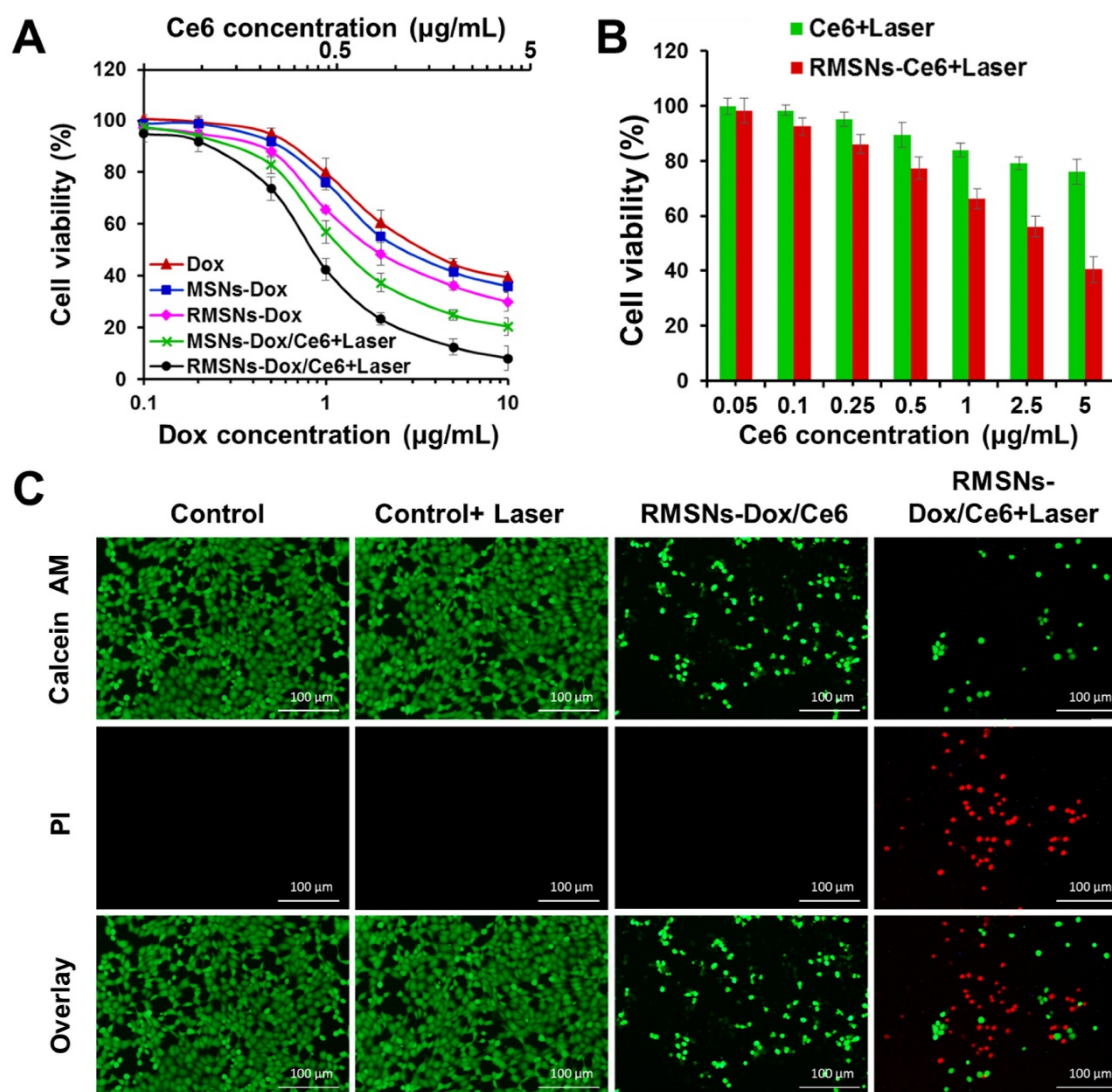


Figure 3. *In vitro* combined chemo-photodynamic therapy of RMSNs-Dox/Ce6 in 4T1 cells. (A) *In vitro* cytotoxicity of different Dox formulations for 24 h incubation at different concentrations, respectively. Data were presented as mean \pm SD (n = 6). (B) The cell viability of 4T1 cells after photodynamic treatment with free Ce6 and RMSNs-Ce6, respectively. Data were presented as mean \pm SD (n = 6). (C) fluorescence images of 4T1 cells after chemo-photodynamic treatment. Viable cells were stained with calcein-AM, and dead/late apoptosis cells were floating and eluted, or stained with PI. Scale bar = 100 μ m.

Figure 2C revealed that after 1, 2 and 4 h incubation, RMSNs-Dox/Ce6 with laser irradiation could induce 1.9-, 2.0-, 2.0-fold enhancement of Dox accumulation compared to that without laser, respectively (Figure 2C). The laser-triggered enhancement of RMSNs-Dox/Ce6 distribution in cells could be because the laser-triggered ROS from Ce6 in RMSNs-Dox/Ce6 would oxidize the adjacent unsaturated phospholipid molecules in the RBC membrane as well as the cancer cell membrane, form defects and affect the permeabilization of cell membrane, leading to the increased cellular uptake of nanoparticles and Dox release from the nanoparticles [41].

***In vitro* chemo-photodynamic therapy of RMSNs-Dox/Ce6**

The cytotoxicity of all Dox-loaded formulations or carriers was evaluated by sulforhodamine B staining (SRB) assay (Figure 3A-B). For photodynamic treatment, cells treated with blank RMSNs, free Ce6, RMSNs-Ce6, MSN-Dox/Ce6 or RMSNs-Dox/Ce6 for 4 h were irradiated with a 655nm laser at 2 W/cm² for 5 min. After 24 h incubation, blank MSNs, RMSNs, and RMSNs+Laser showed negligible cytotoxicity in 4T1 cells, indicating the good compatibility of MSNs and RMSNs even at the MSNs concentration of 25 μ g/mL, as well as laser irradiation alone in 4T1 cells (Figure S8). RMSNs-Dox displayed higher cytotoxicity than that of free Dox. The similar result

was observed in the photocytotoxicity experiment of Ce6 in 4T1 cells. Ce6 at the concentration of 5 µg/mL killed 40.4% cells in RMSNs-Ce6 and 75.9% cells in free Ce6 group (Figure 3B), respectively. These results demonstrated RMSNs-Dox and RMSNs-Ce6 could improve the cytotoxicity of Dox and the photocytotoxicity of Ce6 upon laser irradiation, respectively. This could be due to the slightly enhanced drug uptake of nanoparticles than the free ones (Figure 2A). RMSNs-Dox and RMSNs-Dox/Ce6+Laser showed the significantly enhanced cytotoxicity of 4T1 cells compared to MSNs-Dox and MSN-Dox/Ce6+Laser, respectively. The IC₅₀ values of Dox against 4T1 cells was 2.6 µg/mL for RMSNs-Dox and 0.9 µg/mL for RMSNs-Dox/Ce6+Laser, which was 1.4- and 1.5-fold lower than that of MSNs-Dox (3.7 µg/mL) and MSN-Dox/Ce6+Laser (1.6 µg/mL), respectively. This was probably because RBC membrane coating could prevent premature drug release of MSNs, leading to efficient Dox distribution in 4T1 cells. RMSNs-Dox/Ce6+Laser also showed the most effective cell killing ability compared to both free Dox and RMSNs-Dox groups as expected, the IC₅₀ of which was 5.0- and 2.8-fold lower than that of free Dox (4.5 µg/mL) and RMSNs-Dox (2.6 µg/mL), respectively. The results demonstrated RMSNs-Dox/Ce6 could prevent premature drug release, trigger efficient intracellular Dox distribution, and integrate PDT and chemotherapy to efficiently kill 4T1 cells under laser irradiation.

To further visualize the efficiency of RMSNs-Dox/Ce6, 4T1 cells incubated with RMSNs-Dox/Ce6 were treated with or without laser irradiation at 2 W/cm² for 5 min. Cells were then stained with calcein-AM and PI to identify live and dead/late apoptotic cells, respectively. As shown in Figure 3C, laser irradiation alone showed negligible effect on cell viability, suggesting laser illumination at power density of 2 W/cm² was safe for 4T1 cells. On the other hand, cells incubated with RMSNs-Dox/Ce6 for 24 h caused 75.2% cell death, and significantly decreased cell density was observed. Similar results were also observed in cells treated with RMSNs-Dox/Ce6+Laser, which caused cell death up to 92.1% with negligible green spots in the image. The decreased cell intensity could be due to the cytotoxicity of RMSNs-Dox/Ce6, which induced the cell apoptosis and detachment from the plate. These results indicated that RMSNs-Dox/Ce6 could integrate the synergetic effect of chemotherapy and photodynamic therapy under laser stimuli, leading to the most efficient cell killing capacity.

In vivo blood retention behavior of RMSNs-Dox/Ce6

To investigate the role of the coated RBC membrane on the blood retention of MSNs-Dox/Ce6, we conducted the pharmacokinetic experiment of RMSNs-Dox/Ce6. The blood of the same rats was chosen for RMSNs-Dox/Ce6 fabrication to avoid immune reaction caused by blood cell type inconformity [42]. SD rats were *i.v.* administrated with free Dox, MSNs-Dox/Ce6 and RMSNs-Dox/Ce6 at Dox dose of 5mg/kg, respectively. As shown in Figure 4A, free Dox exhibited a rapid elimination from the blood circulation, with undetectable fluorescence signal after 6h. RMSNs-Dox/Ce6 showed remarkably enhanced blood retention of Dox in comparison with free Dox and MSNs-Dox/Ce6. The elimination half-time ($T_{1/2}$) of RMSNs-Dox/Ce6 was 18.2 h, 9.4- and 67.2- fold higher than that of MSNs-Dox/Ce6 (1.9 h) and free Dox (0.27 h), respectively (Table S1, supporting information). In addition, compared to MSNs-Dox/Ce6, other significantly changed Dox pharmacokinetic parameters were also observed, such as higher area under the curve ($AUC_{(0-\infty)}$), mean residence time ($MRT_{(0-\infty)}$), and significantly lower total clearance (CL). These results indicated the RBC membrane coating could significantly prolong the circulation time of MSNs, which was probably due to the immune-evasive ability of the RBC membrane protein, as well as the membrane protection of the loaded Dox from premature release.

We further evaluated the hematological biocompatibility of RMSNs-Dox/Ce6. As shown in Figure S9, MSNs-Dox/Ce6 induced significantly hemolytic effect at elevated concentrations, which could be due to the large amount of Si-OH on the surface of MSNs and their stellate morphology [43, 44]. In contrast, RMSNs-Dox/Ce6 exhibited much lower hemolytic effect. At a high MSN concentration of 250 µg/mL, the hemolysis percentage of RMSNs-Dox/Ce6 was only 7.5%, significantly lower than that of MSNs-Dox/Ce6 (49.1%). This result showed that the RBC membrane coating could reduce the toxicity of MSNs on red blood cells, which was probably due to the much-decreased Si-OH amounts exposed in the blood, and the changed morphology of MSNs. These results suggested that RMSNs-Dox/Ce6 could provide a safe and sustained drug delivery in blood circulation. We believed the abundant RBC membrane proteins on the surface of RMSNs could prevent immune attack and displayed low immunogenicity, these proteins, however, could also be a immunogenic construct as they are targets of the autoimmune hemolytic anemia. For further clinical applications, such kind of RBC-mimetic nanoparticles

still remained to be carefully checked for their immunogenicity, and allogeneic RBCs should not be used for fabrication, as the alloantigen might cause higher risk of immunoreaction.

In vivo imaging and improved biodistribution profile of RMSNs-Dox/Ce6

Benefited to the strong fluorescence emission of Ce6 in the deep-red light region, the *in vivo* biodistribution of RMSNs and MSNs was investigated in a 4T1 orthotopic 4T1 cancer spontaneous mouse model (Figure 4B-C). Mice injected with MSNs-Ce6 formulation showed slight signals at peritumor site at 1 h post administration and rapidly decreased, and revealed negligible signals at 24 h after *i.v.* injection, which could be due to the recognition of the reticulo-endothelial system (RES), as well as the leakage of Ce6 from the nanoparticles, resulting in a rapid clearance from the circulation system. Mice injected with RMSN-Ce6 showed significantly enhanced and sustained fluorescence distribution in tumor sites compared to MSN-Ce6 groups. At 4 h post

injection, the fluorescence signals reached the maximum. Then, the fluorescence intensity dropped slowly over time due to blood clearance, which could be because the RBC membrane coating could protect the encapsulated Ce6 from premature leakage, as well as evade the immune system to obtain a long circulation time, leading to enhanced tumor distribution *via* EPR effect. Afterwards, the *ex vivo* biodistribution of RMSNs-Ce6 was examined in 4T1 tumor bearing mice using fluorescence imaging (Figure 4B). At 24 h after administration, MSNs-Ce6 mainly distributed in liver, lung and kidney, with negligible fluorescence in the tumor, implying clearance by renal filtration and macrophage cells. In contrast, RMSNs-Ce6 displayed significantly decreased fluorescence intensity in the liver, spleen and kidney compared to MSN-Ce6, respectively. These results demonstrated that RMSNs-Ce6 could improve the biodistribution of MSNs-Ce6 by RBC membrane camouflaging, and proved as an effective fluorescence probe for *in vivo* tumor imaging.

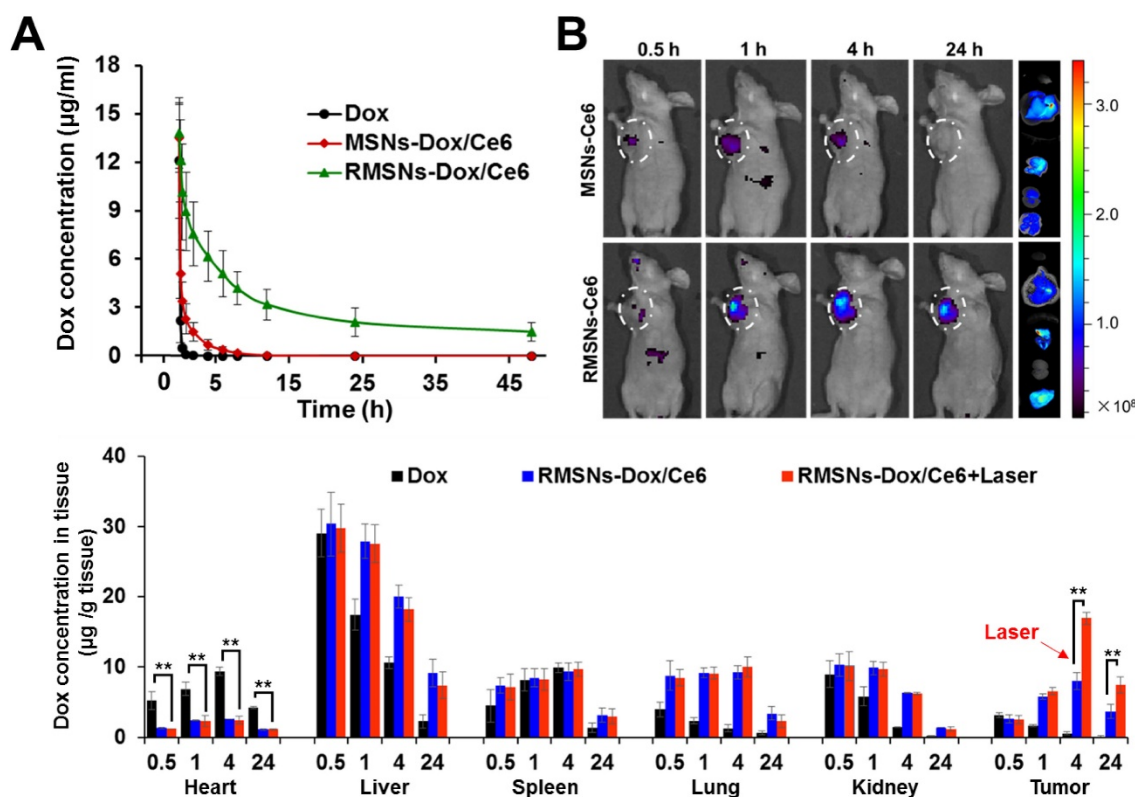


Figure 4. The *in vivo* pharmacokinetic behaviors and improved biodistribution profile of RMSNs-Dox/Ce6. (A) The pharmacokinetic behaviors of free Dox, MSNs-Dox/Ce6 and RMSNs-Dox/Ce6 in rats after *i.v.* administration at Dox dose of 5 mg/kg. Data were presented as mean \pm SD (n = 3) (B) Fluorescence images of 4T1 tumor-bearing mice *i.v.* injected with MSNs-Ce6 and RMSNs-Ce6 at different time points, and *ex vivo* Ce6 distribution in major organs and tumors examined at 24 h post injection (from top to bottom: heart, liver, spleen, lung, kidney, tumor), respectively (Ce6 dose of 2.5 mg/kg). (C) Quantitative analysis of Dox biodistribution in tissues and tumors of tumor-bearing mice injected with free Dox, RMSNs-Dox/Ce6 and RMSNs-Dox/Ce6+laser at a Dox dose of 5 mg/kg, respectively. The red arrow indicated the time points of laser irradiation. Data were presented as mean \pm SD (n = 3), ***P* < 0.01.

Inspired by the above results, we further investigated the biodistribution of Dox in RMSNs-Dox/Ce6 in the 4T1 tumor-bearing mice (Figure 4C). 4 h was chosen as the time point for laser irradiation. As continuing exposure of mice to near-infrared light might cause protein dehydration and electrokinetic potential change of erythrocytes in circulation, the laser irradiation time was limited to 5 min only at the tumor position [45-47]. Free Dox was set as a control, for RMSN-Dox/Ce6+Laser group, mice were irradiated by a laser at power of 2 W/cm² for 5 min at the tumor site at 4 h after *i.v.* injection of RMSN-Dox/Ce6. Free Dox was widely distributed into major organs and rapidly eliminated. The accumulation of Dox in tumor was negligible after 4 h. However, in RMSN-Dox/Ce6 group, the Dox distribution in the heart was significantly decreased, while the accumulation in tumor and lung was greatly enhanced at all time-points, which could be helpful for the treatment of the primary tumor and the lung metastases, as well as decreasing the cardiotoxicity of Dox. This could be due to the enhanced EPR effect and the decreased RES capture. Furthermore, under a laser stimuli, the tumor accumulation of Dox in RMSN-Dox/Ce6 was greatly enhanced, which was 2.0- and 2.1-fold higher than that without laser irradiation. The laser-activated tumor-specific Dox accumulation was probably attributed to two reasons. Firstly, the laser-triggered ROS generation from Ce6 in RMSNs-Dox/Ce6 could destroy the permeabilization of tumor cell membranes, leading to enhanced penetration and cellular uptake of Dox in tumor sites. Secondly, the ROS could also form defects of the RBC membrane, leading to rapid Dox release and wide distribution in the tumor sites.

In vivo anticancer and anti-metastasis efficacy

The ability of RMSNs-Dox/Ce6 combined with laser irradiation to inhibit the growth of the primary tumor and lung metastases was investigated in nude mice bearing orthotopic 4T1 breast tumors. When the tumor volume reached 100 mm³, mice were injected with different formulations or carriers at a Dox dose of 5 mg/kg and a Ce6 dose of 2.5 mg/kg. Illumination treatment was performed at 4 h after *i.v.* injection. Two mice groups (saline and RMSNs+Laser) were set as controls. As shown in Figure 5A and Figure S10, at the end of experiment, the tumor volume and the tumor weight of the free Dox-treated group were 68.4% and 67.8% of the control group, respectively. The addition of Ce6 plus irradiation slightly enhanced the tumor inhibitory effect, with 43.8% and 44.6% reduction in tumor volume and tumor weight at the end of 22 days, respectively. After Dox and Ce6 were co-loaded in MSNs, MSNs-Dox/Ce6+Laser showed

56.3% and 59.7% reduction of tumor volume and tumor weight compared to those of the control group, respectively. After RBC membrane coating, the highest antitumor efficacy was achieved in RMSN-Dox/Ce6+Laser group, with complete inhibition of the tumor growth from day 13. The tumor volume was only 6.1% compared to those of the saline group, which was 9.2- and 7.2-fold lower than that of Dox/Ce6+Laser and MSNs-Dox/Ce6+Laser, respectively. This enhanced anticancer efficacy could be because the RBC membrane coating could improve the circulation time of the encapsulated therapeutic agents, protect them from leakage, and lead to improved drug accumulation in the tumor *via* EPR effect (Figure 4A-B). On the other hand, the RMSNs-Dox/Ce6+Laser group also showed superior reduction of tumor volume compared to RMSNs-Dox (28.2%) and RMSNs-Ce6+Laser (34.6%) groups, which was 5.7- and 4.6-fold lower than that of RMSNs-Ce6+Laser and RMSNs-Dox groups, respectively. The tumor inhibition rate of RMSNs-Dox/Ce6 was 91.4%, which was significantly higher than RMSNs-Ce6+Laser (68.9%) and RMSNs-Dox (73.7%), respectively. These results indicated the dramatically enhanced antitumor efficacy of the combined chemo-photodynamic therapy of RMSN-Dox/Ce6+Laser than the mono chemotherapy or photodynamic therapy. The body weights were also measured to investigate the systemic toxicity. As shown in Figure 5B, free Dox and Dox/Ce6+Laser showed rapidly decreased body weights, but the weight recovered to the normal level at the end. Other groups exhibited slightly increased body weights, indicating low systemic toxicity of these formulations.

The mechanism of the antitumor effect of RMSN-Dox/Ce6+Laser was further exploited by TUNEL staining of excised tumors. As shown in Figure 5D, the degree of apoptosis was consistent with that of the tumor inhibition. Non-apoptosis fluorescence signal was observed in saline group. Dox and Dox/Ce6+Laser groups showed certain apoptosis, MSNs-Dox/Ce6+Laser, RMSNs-Dox and RMSNs-Ce6+Laser groups exhibited considerable apoptosis, and the RMSNs-Dox/Ce6+Laser group showed the maximum range of apoptosis fluorescence, which indicated that the efficient suppression of tumor growth resulted from RMSNs-Dox/Ce6 and Laser- induced apoptosis of tumor cells.

Since the 4T1 tumor is a high spontaneous lung metastasis breast tumor, the anti-metastasis effect was also evaluated (Figure 6A-B). Wide metastases tumor burden was observed in the lung of the saline group,

with average metastatic foci of 55, confirmed by hematoxylin and eosin (H&E) staining. Dox and Dox/Ce6+Laser showed fewer range of metastases burden, with average metastatic nodules of 33.6 and 32.5, respectively. The metastatic foci of MSNs-Dox/Ce6, RMSNs-Dox and RMSNs-Ce6+Laser groups was reduced to 14.5, 8.7 and 12.5, which was 56.9%, 73.3% and 75.1% fewer than that of the saline group, respectively. This could be benefited from the drug distribution in the primary tumor, and the lung with metastases. RMSNs-Dox/Ce6 with combination of laser irradiation significantly enhanced the anti-metastatic efficacy, with no metastatic foci found in the lung, which was confirmed by the H&E staining. This could be attributed to the most effective inhibition of the primary tumor growth and the complete suppression of lung metastasis occurrence. Taken together, RMSNs-Dox/Ce6 combined with laser irradiation could provide a synergetic effect of the chemo-photodynamic therapy, to completely

suppress the growth of the primary tumor and lung metastases of breast cancer.

Histological analysis

At the end of the anticancer experiment, major organs were excised and investigated by histopathological analysis (Figure 7). Obvious accumulation of neutrophils in the heart was observed in the free Dox and Dox/Ce6+Laser groups compared to the saline group, indicating apparent cardiotoxicity caused by free Dox. Non-evident pathological change was detected in the slices of heart, liver, spleen and kidney of RMSN-Dox and RMSNs-Dox/Ce6+laser groups, indicating that the nanoparticle formulation and the RBC membrane coating could decrease the cardiac toxicity caused by Dox, which was probably due to the reduced accumulation of Dox in the heart. This results suggested that RMSNs-Dox/Ce6+Laser could effectively suppress the tumor growth and pose no obvious signals of toxic side-effects in mice.

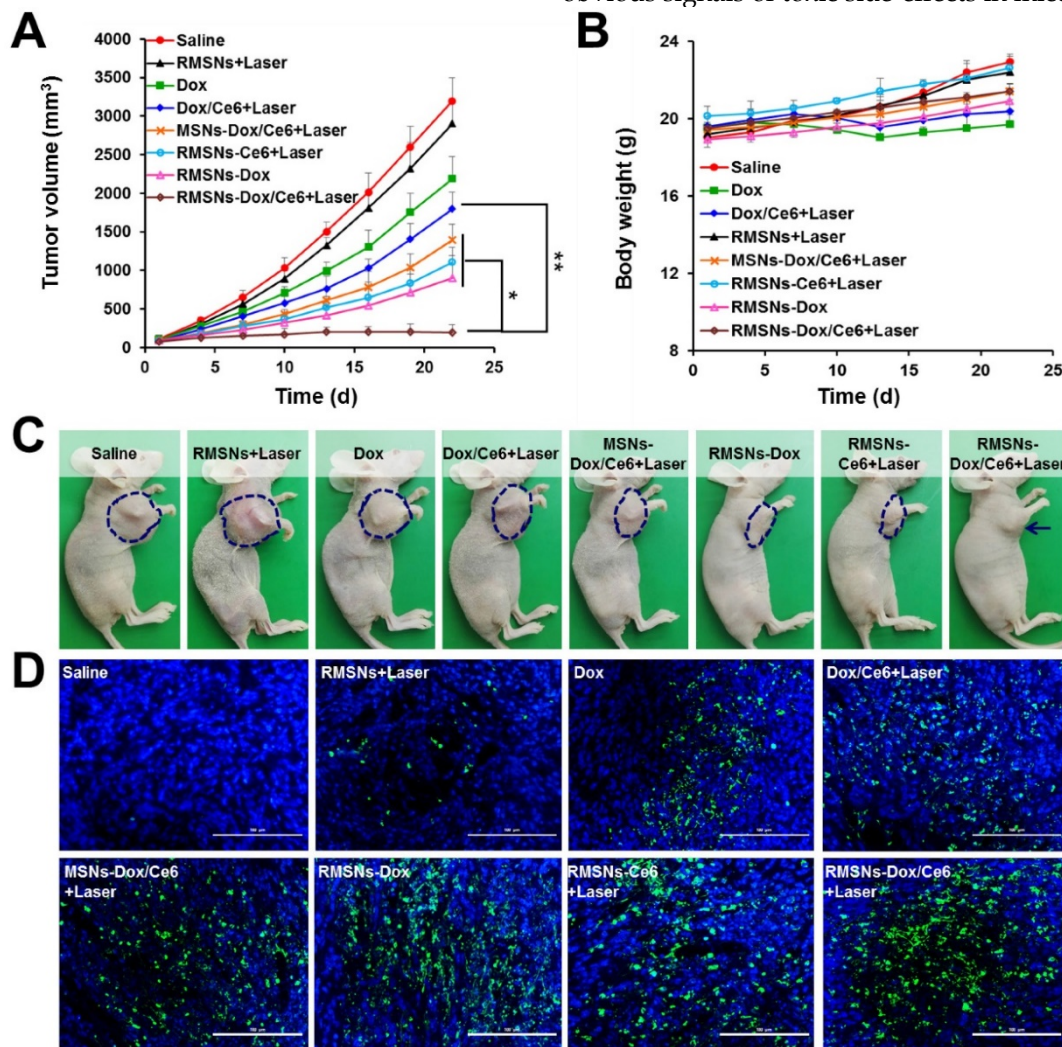


Figure 5. *In vivo* antitumor effect in 4T1 tumor bearing mice. (A) Tumor growth curve after *i.v.* injection of different formulations. (B) Body weights of 4T1 tumor-bearing mice. (C) Representative photos of tumor-bearing mice at the end of the experiment. (D) Representative images (200 ×) of TUNEL examination of tumor sections treating with different formulations. Scale bar = 100 μm. Data were presented as mean ± SD (n = 6), *P < 0.05, **P < 0.01.

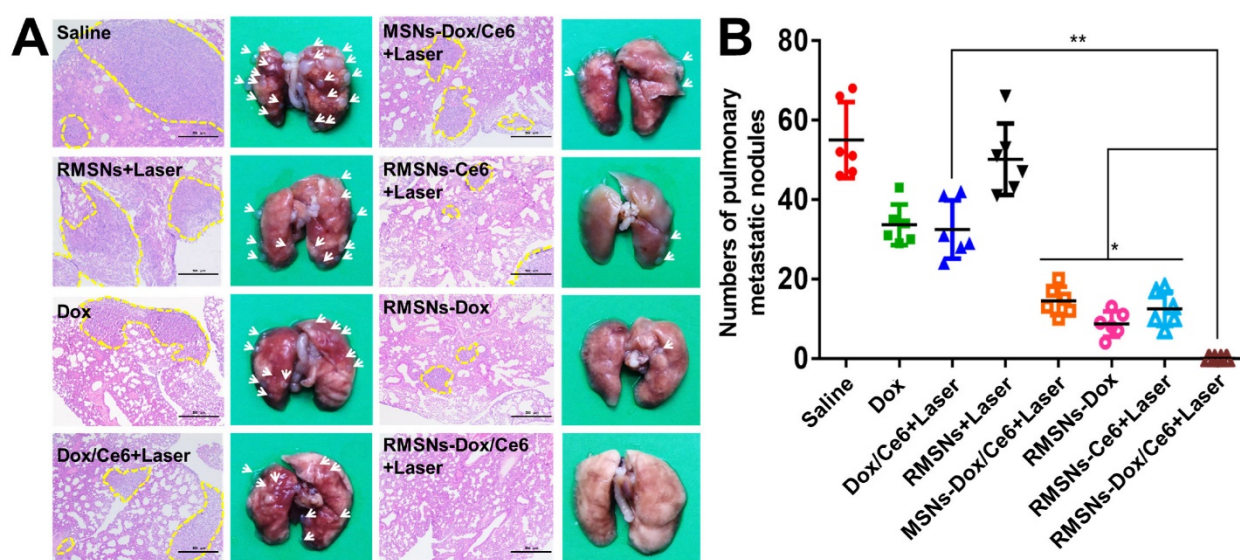


Figure 6. *In vivo* antimetastasis effect in 4T1 tumor bearing mice. (A) Representative microphotos (left) and H&E stained sections (right) of lungs in different groups. Yellow circles indicated the pulmonary metastases, scale bar = 500 μ m. (B) Analysis of the pulmonary metastasis nodules in different groups. Data were presented as mean \pm SD (n = 6), * P < 0.05, ** P < 0.01.

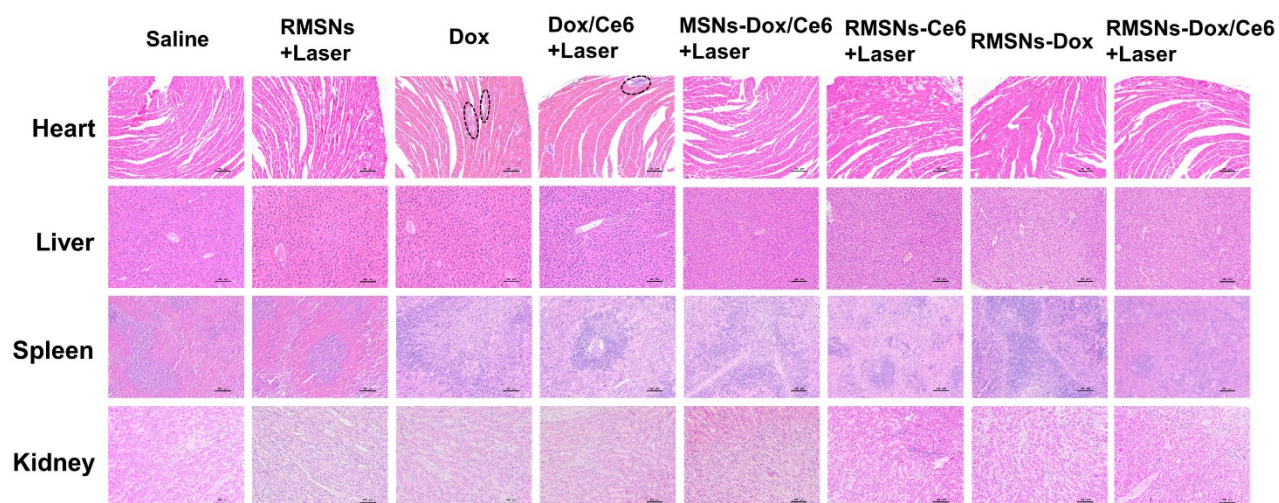


Figure 7. H&E staining of heart, liver, spleen and kidney (100 \times) at the end of the antitumor inhibition test. The black circles indicated the inflammation in the heart of the Dox-treated mice. Scale bar = 100 μ m.

Conclusion

In summary, we aimed at the easy aggregation in saline buffers and the limited circulation lifetime of current MSNs, fabricated the laser-responsive MSNs supported RBC-mimetic nanoparticles with long time circulation and controlled tumor-specific drug release, to realize efficient anticancer drug delivery. The coated RBC membrane could greatly enhance the colloidal stability of the supported MSNs, and protect the encapsulated Dox and Ce6 from premature release in the bloodstream. Benefited from the strong fluorescence of Ce6, RMSNs-Dox/Ce6 could be applied as a tumor imaging probe *in vivo*. Utilizing an external laser, the generated ROS from Ce6 in the RMSNs-Dox/Ce6 could destroy the RBC membrane, leading to an effectively enhanced Dox release profile.

Besides, ROS could also destroy the permeabilization of tumor cell membranes, suggesting the tumor-specific cellular uptake and penetration of RBC-mimetic MSNs. In a metastatic 4T1 breast cancer mouse model, RMSNs-Dox/Ce6 completely suppressed the primary tumor growth and inhibited metastasis occurrence. These findings suggested the great potential of MSNs-supported RBC-mimetic nanoparticles for efficient antimetastasis therapy, which offered a new direction for MSNs optimization.

Experimental Methods

Materials

Doxorubicin (Dox) hydrochloride was purchased from Hisun Pharmaceutical Co. Ltd., (Zhejiang, China). Chlorin e6 (Ce6) was obtained from

J&K Scientific Ltd., (Shanghai, China). Monodisperse Mesoporous Silica Nanosphere-Stellate MSNs (MSNs) was purchased from XFNano (Nanjing, China). Trypsine-EDTA, fetal bovine serum (FBS) and phosphate buffered solution (PBS) were purchased from Gibco-BRL (Burlington, Canada). The RPMI 1640 medium and hoechst 33342 were obtained from Yeasen (Shanghai, China). Singlet oxygen sensor green reagent, propidium iodide (PI), Reactive oxygen species assay kit and LIVE/DEAD Viability/Cytotoxicity Kit were purchased from Invitrogen (Oregon, USA). Protease inhibitor cocktail (EDTA-Free, 100× in DMSO) was obtained from SelleckChem (Houston, USA). Other chemicals if not mentioned were analytical grade and obtained from Sinopharm Group Chemical Reagent Co., Ltd. (Shanghai, China). Ultrapure water was produced with a Milli-Q water purification system. All glassware was rinsed extensively with ultrapure water and dried before use.

Cell culture

4T1 mouse mammary tumor cells and mouse macrophage RAW 264.7 cells were obtained from Cell Bank of Shanghai, Chinese Academy of Sciences (Shanghai, China). 4T1 Cells were cultured in RPMI 1640 containing 10% fetal bovine serum (FBS), 2.5g/L glucose, 0.11 g/L Sodium Pyruvate, 100 U/mL penicillin G sodium and 100 mg/mL streptomycin sulfate (complete 1640 medium). RAW264.7 cells were grown in DMEM supplemented with 10% FBS, 100 U/mL penicillin G sodium and 100 mg/mL streptomycin sulfate. Both 4T1 and RAW264.7 cells were maintained at 37°C in a humidified and 5% CO₂ incubator.

Animals

Female BALB/c nude mice and BALB/c mice (18-20g) were purchased from Shanghai Experimental Animal Center (Shanghai). All procedures about animals were carried out under the guideline approved by the Institutional Animal Care and Use Committee (IACUC) of the Shanghai Institute of Materia Medica, Chinese Academy of Sciences.

Preparation of Ce6 loaded MSN (MSNs-Ce6) and Dox loaded MSNs-Ce6 (MSNs-Dox/Ce6)

To prepare the Ce6 loaded MSN (MSNs-Ce6), the Ce6 solution (10 mg dispersed in PBS) was dropwise added to 10 mL distilled water containing 10 mg MSN slowly, and stirred at room temperature overnight to reach the equilibrium state. The resulting solution was then centrifuged at 8000 rpm for 10 min, and washed with distilled water to remove the physically adsorbed Ce6. Dox loaded MSNs (MSNs-Dox) was prepared with the same procedure

of MSNs-Ce6. To prepare the Ce6 and Dox co-loaded MSNs (MSNs-Dox/Ce6), Dox (10 mg) and Ce6 (10 mg) dissolved in distilled water was dropwise added to 10 mL distilled water containing 10 mg MSN, and stirred at room temperature for 24 h, and then washed with distilled water to remove the unbounded Ce6 and Dox. The resulting nanoparticles solution was filtrated through a 0.22 µm filter (Millipore, USA) before use.

Preparation and characterization of RMSNs-Dox/Ce6

Firstly, red blood cell-mimetic vesicles (RVs), which were devoid of cytoplasmic contents, were prepared according to our previous report [42, 48]. To prepare RMSNs-Dox/Ce6, RVs were coated onto MSNs-Dox/Ce6 by co-extruding through a 200nm polycarbonate membrane for at least 10 passes. Blank RMSNs, RMSNs-Dox without Ce6 and RMSNs-Ce6 without Dox were prepared with corresponding procedure as RMSNs-Dox/Ce6. The particle size and Zeta potential were measured using a Malven zetasizer ZEN3690 analyzer (Malven, UK).

A transmission electron microscopy (TEM, Tecnai G2 F20 S-TWIN, FEI, Hillsboro, Oregon, USA) was used to examine the surface morphology of RMSNs-Dox/Ce6. Samples were placed on copper grid with films and air-dried before imaging. The morphologic changes of RMSNs-Dox/Ce6 in response to laser irradiation was visualized by irradiating the nanoparticles solution with a 655nm laser (Changchun New Industries Optoelectronics Tech. Co., Ltd, Changchun, China) for 5 min at a power output of 2 W cm⁻², then immediately performed by TEM.

The stability of MSNs-Dox/Ce6 and RMSNs-Dox/Ce6 in physical environment was simulated by dispersing 1 mg MSNs-Dox/Ce6 and RMSNs-Dox/Ce6 in 1640 medium containing 10% FBS for two weeks, respectively. Their particle sizes were measured at different time points by a Malven zetasizer ZEN3690 analyzer.

To examine the photoactivity of Ce6 in RMSNs-Dox/Ce6, RMSNs-Dox/Ce6, RMSNs-Ce6 and Ce6 solution with a Ce6 concentration of 10 µg/mL was added with the ROS probe singlet oxygen sensor green (SOSG) according to the manufacture's protocol, respectively. The blank RMSNs were used as a control. The solution was then illuminated with a 655nm laser (Changchun New Industries Optoelectronics Tech. Co., Ltd., Changchun, China) at 2 W cm⁻². At appropriate points, the ROS generation was determined by measuring the fluorescence of SOSG (excitation = 525 nm).

The in vitro Dox release profile of

RMSNs-Dox/Ce6 was carried out by dialysis method. 1 mL of RMSNs-Dox/Ce6 and MSNs-Dox/Ce6 containing 0.5 mg Dox was added into dialysis bag (MWCO= 14000) and sealed, respectively. Then these bags were kept in 1× PBS (pH=7.4 or 5.0) under horizontal shaking at 100 rpm for 48 h. To investigate the stimuli effect of laser irradiation on the release behavior, the release experiment of RMSNs-Dox/Ce6 was performed with or without 2 W cm⁻² 655 nm laser irradiation for 5 min at different time points at 37 °C. At appropriate time point, 100 µl of different samples was collected, and a microplate reader (Infinite F200, TECAN, Austria) was used to monitor the released Dox content. To visualize the release behavior, at the end of the release experiment, the fluorescence intensity of Dox and Ce6 in RMSNs-Dox/Ce6 solution was imaged under the Image Lab system (Bio-Rad, USA), respectively. Free Dox and Ce6 with or without laser illumination were set as controls, respectively. To avoid the fluorescence interference of Ce6 to that of Dox, the fluorescence of Dox was determined at excitation wavelength of 488 nm and that of Ce6 was 654 nm.

The drug-loading ratio (DL%) and encapsulation efficiency (EE%) of RMSNs-Dox/Ce6 were analyzed according to the fluorescence intensity of Dox and Ce6 by a microplate reader, which were calculated by the following formula: DL (%) = ((weight of recovered drug)/(weight of nanoparticles)) ×100; EE (%) = ((weight of recovered drug)/(weight of initially added drug)×100.

ROS generation *in vitro* and cellular uptake of nanoparticles

The laser-induced ROS generation experiment was performed by the Reactive Oxygen Species assay kit according to the manufacturer's instructions. Briefly, 4T1 cells were seeded in 24-well plates at 8×10⁴ cells/well. After 24 h incubation, free Dox, MSNs-Dox/Ce6 and RMSNs-Dox/Ce6 were added to the 4T1 cells at a Ce6 concentration of 3 µg/mL, and a Dox concentration of 10µg/mL for 4 h, respectively. Then the cell culture medium was refreshed and added with 10µM of fluorescent probe DCFH-DA and 1µg/well Hoechst 33342. RMSNs-Dox/Ce6-incubated cells were then treated with a 655nm laser for 5 min at different laser powers. Cells were visualized under a confocal laser scanning microscopy (CLSM, Olympus Fluoview 1000, Japan). To further qualify the ROS generation, cells were washed, harvested and resuspended in PBS, and the fluorescence analysis was acquired by a FACSCalibur system (Becton Dickinson, USA).

To evaluate the photodynamic influence on cellular distribution of Dox, the 4T1 cells were treated

with free Dox and different nanoparticles at a Dox concentration of 10 µg/mL for 1, 2 and 4 h, respectively. Cells incubated with RMSNs-Dox/Ce6 (3 µg/mL Ce6 and 10 µg/mL Dox) were exposed to 2 W cm⁻² 655 nm laser irradiation for 5 min. After 30 min, cells were washed with PBS, and the fluorescence was monitored by a microplate reader (Infinite F200, TECAN, Austria).

In vitro chemo/phototoxicity of RMSNs-Dox/Ce6

To determine the chemo/phototoxicity of RMSNs-Dox/Ce6, 4T1 cells were seeded in 96-well plates at 4×10³ cells/well overnight. Then, medium was removed and replaced by fresh media including various concentrations of free Dox and different nanoparticles, respectively. The final concentrations of Dox ranged from 1.0×10⁻⁴ to 0.01 mg/mL. For MSN-Dox/Ce6+L, RMSNs+L and RMSNs-Dox/Ce6+L group, cells were irradiated with a 2 W cm⁻² 655 nm laser for 5 min after 4 h incubation, respectively. Cells incubated with MSNs, RMSNs, and RMSNs+L were used as controls. To determine the phototoxicity of free Ce6 and Ce6-loaded RMSNs-Ce6, cells were incubated with Ce6 of different concentration ranging from 1.0×10⁻⁴ to 0.01 mg/mL, and irradiated with a 2 W cm⁻² 655 nm laser for 5 min after 4 h. After 24 h incubation, cell cytotoxicity was calculated by the sulforhodamine B staining assay through a microplate reader (Infinite F200, TECAN, Austria). Each group was repeated in sextuplicate.

To further visualize the cell chemo/phototoxicity of RMSNs-Dox/Ce6 treatment, 4T1 cells were seeded in 96-well plates at 5×10³ cells/well and incubated overnight. Then medium was replaced with fresh media, and added with RMSNs-Dox/Ce6. After 4h incubation, cells were irradiated with the 655nm laser at a power density of 2 W cm⁻² for 5 min. Cells without nanoparticles treatment were irradiated as control. After 24 h, all cells were washed with PBS, treated with Calcein AM and PI according to the manufacturer's protocol, and detected under a fluorescent microscope (IX81, Olympus, Japan).

In vivo imaging and laser-triggered Dox distribution of RMSNs-Dox/Ce6

Owing to the strong fluorescence emission in the deep-red light region, the biodistribution of RMSNs-Dox/Ce6 experiment was conducted by fluorescence imaging analysis in a well-established spontaneous 4T1 mouse breast metastatic cancer model. Tumor-bearing Balb/c nude mice were randomly divided into two groups when the tumor

volume reached 200-400 mm³, and intravenously injected with MSNs-Dox/Ce6 and RMSNs-Dox/Ce6 (Ce6 of 3 mg/kg), respectively. At 0.5, 1, 4 and 24 h after injection, mice were anesthetized and imaged under the IVIS imaging system (Xenogen, Alameda, CA). At the end of the experiment, mice were sacrificed, and major organs were collected, rinsed with cold PBS and imaged by the IVIS imaging system.

To investigate the *in vivo* Dox biodistribution of RMSNs-Dox/Ce6, female Balb/c nude mice bearing 4T1 tumors were intravenously injected with free Dox, RMSNs-Dox/Ce6 (Dox of 5 mg/kg). To evaluate the PDT effect on Dox distribution of RMSNs-Dox/Ce6 *in vivo*, tumors were irradiated by the 655nm laser at 2 W cm⁻² for 5 min in RMSNs-Dox/Ce6 group at 4 h after injection. At different time points, mice were sacrificed, and major organs were collected, rinsed with cold PBS. For further quantitative analysis, the weighed tissues were mixed with DMSO, homogenized, and centrifugation at 1×10⁴ rpm for 10 min. The supernatants were collected and measured for the content of Dox using a microplate reader (excitation = 479 nm).

In vivo antitumor and anti-metastasis efficacy

The tumor inhibition experiment was conducted in a 4T1 spontaneous 4T1 mouse breast metastatic cancer model. Mice were randomly assigned to six groups (n=6). 100 µl of 4T1 cell suspension (2×10⁵ cells) was injected into the right mammary gland of nude mice to develop the spontaneous metastasis model. When the tumor volume reached 50-100 mm³, mice were treated with saline, Dox, RMSNs+Laser, the mixture of Dox and Ce6 in combination of laser illumination (Dox/Ce6+Laser), RMSNs-Ce6+Laser, RMSNs-Dox and RMSNs-Dox/Ce6+Laser (Dox of 5mg/kg, Ce6 of 2.5 mg/kg). At 4 h after injection, for laser groups, tumors of mice were irradiated by a 655nm laser at 2 W cm⁻² for 5 min. The treatment was repeated every two days for eight times. Body weight and tumor volume were measured every time after injection. The tumor volume was analyzed by this formula: $V = L \times W \times W / 2$ (L, longest dimension; W, shortest dimension). At 22 day, animals were sacrificed, major organs were immediately excised, washed with cold PBS and fixed with 4% formalin. The tumors were photographed and weighted. The tumors were then embedded in paraffin, subjected to the fluorescence TUNEL assay to measure the intratumoral late apoptosis, and also stained by hematoxylin and eosin (H&E) for the apoptosis and necrosis evaluation. The pulmonary metastatic nodules were counted to detect the micrometastatic

foci, and lungs were stained by H&E for histopathological analysis. Images were observed under a fluorescence microscope (Olympus, Japan). To observe the systemic toxicity of all the Dox formulations, heart, liver, spleen and kidney were excised, stained by H&E and imaged by a fluorescence microscope (Olympus, Japan).

Statistical analysis

The mean values ± SD was determined for each treatment group and each value represented the mean of at least three repetitive experiments in each group. Non-parametric test was performed using IBM SPSS statistics to assess the significance of the difference between two groups, **p* < 0.05 and ***p* < 0.01.

Supplementary Material

Experimental methods and results, supplementary figures and tables.

<http://www.thno.org/v07p0523s1.pdf>

Acknowledgements

The National Natural Science Foundation of China (81521005 and 81630052), Key Research Projects of the Frontier Science of the Chinese Academy of Sciences (QYZDJ-SSW-SMC020) and the National Basic Research Program of China (2014CB931902) are gratefully acknowledged for the financial support.

Competing Interests

The authors have declared that no competing interest exists.

References

1. Siegel RL, Miller KD, Jemal A. Cancer statistics, 2015. *Ca-cancer J Clin.* 2015;65:5-29.
2. Xu X, Ho W, Zhang X, et al. Cancer nanomedicine: from targeted delivery to combination therapy. *Trends Mol Med.* 2015;21:223-32.
3. He Q, Shi J. MSN anti-cancer nanomedicines: chemotherapy enhancement, overcoming of drug resistance, and metastasis inhibition. *Adv Mater.* 2014;26:391-411.
4. He C, Liu D, Lin W. Self-assembled core-shell nanoparticles for combined chemotherapy and photodynamic therapy of resistant head and neck cancers. *ACS Nano.* 2015;9:991-1003.
5. Chen Y, Chen H, Shi J. *In vivo* bio-safety evaluations and diagnostic/therapeutic applications of chemically designed mesoporous silica nanoparticles. *Adv Mater.* 2013;25:3144-76.
6. Butler KS, Durfee PN, Theron C, et al. Protocells: modular mesoporous silica nanoparticle-supported lipid bilayers for drug delivery. *Small.* 2016;12:2173-85.
7. Wang LS, Wu LC, Lu SY, et al. Biofunctionalized phospholipid-capped mesoporous silica nanoshuttles for targeted drug delivery: improved water suspensibility and decreased nonspecific protein binding. *ACS Nano.* 2010;4:4371-9.
8. He Q, Zhang Z, Gao F, et al. *In vivo* biodistribution and urinary excretion of mesoporous silica nanoparticles: effects of particle size and PEGylation. *Small.* 2011;7:271-80.
9. Barbé C, Bartlett J, Kong L, et al. Silica particles: a novel drug-delivery system. *Adv Mater.* 2004;16:1959-66.
10. Bouchoucha M, C-Gaudreault R, Fortin MA, et al. Mesoporous silica nanoparticles: selective surface functionalization for optimal relaxometric and drug loading performances. *Adv Funct Mater.* 2014;24:5911-23.
11. Chang B, Chen D, Wang Y, et al. Bioresponsive controlled drug release based on mesoporous silica nanoparticles coated with reductively sheddable polymer shell. *Chem Mater.* 2013;25:574-85.

12. Wu J, Sailor M. Chitosan hydrogel-capped porous SiO₂ as a pH responsive nano-valve for triggered release of insulin. *Adv Funct Mater.* 2009;19:733-41.
13. Vivero Escoto JL, Slowing II, Trewyn BG, et al. Mesoporous silica nanoparticles for intracellular controlled drug delivery. *Small.* 2010;6:1952-67.
14. Li Z, Barnes JC, Bosoy A, et al. Mesoporous silica nanoparticles in biomedical applications. *Chem Soc Rev.* 2012;41:2590-605.
15. Han N, Wang Y, Bai J, et al. Facile synthesis of the lipid bilayer coated mesoporous silica nanocomposites and their application in drug delivery. *Micropor Mesopor Mat.* 2016;219:209-18.
16. Chen WC, Zhang AX, Li SD. Limitations and niches of the active targeting approach for nanoparticle drug delivery. *European Journal of Nanomedicine.* 2012;4:89-93.
17. Yoo JW, Irvine DJ, Discher DE, et al. Bio-inspired, bioengineered and biomimetic drug delivery carriers. *Nature Reviews Drug Discovery.* 2011;10:521-35.
18. Wang C, Sun X, Cheng L, et al. Multifunctional theranostic red blood cells for magnetic-field-enhanced in vivo combination therapy of cancer. *Adv Mater.* 2014;26:4794-802.
19. Sun X, Wang C, Gao M, et al. Remotely controlled red blood cell carriers for cancer targeting and near-infrared light-triggered drug release in combined photothermal-chemotherapy. *Adv Funct Mater.* 2015;25:2386-94.
20. Rao L, Bu LL, Xu JH, et al. Red blood cell membrane as a biomimetic nanocoating for prolonged circulation time and reduced accelerated blood clearance. *Small.* 2015;11:6225-36.
21. Hu CM, Zhang L, Aryal S, et al. Erythrocyte membrane-camouflaged polymeric nanoparticles as a biomimetic delivery platform. *Proc Natl Acad Sci U S A.* 2011;108:10980-5.
22. Rao L, Meng QF, Huang Q, et al. Photocatalytic degradation of cell membrane coatings for controlled drug release. *Adv Healthc Mater.* 2016;5:1420-7.
23. Ding H, Lv Y, Ni D, et al. Erythrocyte membrane-coated NIR-triggered biomimetic nanovectors with programmed delivery for photodynamic therapy of cancer. *Nanoscale.* 2015;7:9806-15.
24. Hu C-MJ, Zhang L, Aryal S, et al. Erythrocyte membrane-camouflaged polymeric nanoparticles as a biomimetic delivery platform. *Proc Natl Acad Sci U S A.* 2011;108:10980-5.
25. Rao L, Bu LL, Cai B, et al. Cancer cell membrane-coated upconversion nanoprobe for highly specific tumor imaging. *Adv Mater.* 2016;28:3460-6.
26. Fang RH, Hu CM, Luk BT, et al. Cancer cell membrane-coated nanoparticles for anticancer vaccination and drug delivery. *Nano Lett.* 2014;14:2181-8.
27. Yu H, Cui Z, Yu P, et al. pH- and NIR light-responsive micelles with hyperthermia-triggered tumor penetration and cytoplasm drug release to reverse doxorubicin resistance in breast cancer. *Adv Funct Mater.* 2015;25:2489-500.
28. Toy R, Bauer L, Hoimes C, et al. Targeted nanotechnology for cancer imaging. *Adv Drug Deliver Rev.* 2014;76:79-97.
29. Li Z, Dong K, Huang S, et al. A smart nanoassembly for multistage targeted drug delivery and magnetic resonance imaging. *Adv Funct Mater.* 2014;24:3612-20.
30. Zhang Z, Wang J, Nie X, et al. Near infrared laser-induced targeted cancer therapy using thermoresponsive polymer encapsulated gold nanorods. *J Am Chem Soc.* 2014;136:7317-26.
31. Du X, Xiong L, Dai S, et al. Intracellular microenvironment-responsive dendrimer-like mesoporous nanohybrids for traceable, effective, and safe gene delivery. *Adv Funct Mater.* 2014;24:7627-37.
32. Polshettiwar V, Cha D, Zhang X, et al. High-surface-area silica nanospheres (KCC-1) with a fibrous morphology. *Angew Chem Int Ed Engl.* 2010;49:9652-6.
33. Zhang K, Xu LL, Jiang JG, et al. Facile large-scale synthesis of monodisperse mesoporous silica nanospheres with tunable pore structure. *J Am Chem Soc.* 2013;135:2427-30.
34. Luk BT, Hu C-MJ, Fang RH, et al. Interfacial interactions between natural RBC membranes and synthetic polymeric nanoparticles. *Nanoscale.* 2014;6:2730-7.
35. Zhang Z, Wang L, Wang J, et al. Mesoporous silica-coated gold nanorods as a light-mediated multifunctional theranostic platform for cancer treatment. *Adv Mater.* 2012;24:1418-23.
36. Allison RR, Downie GH, Cuenca R, et al. Photosensitizers in clinical PDT. *Photodiagnosis Photodyn Ther.* 2004;1:27-42.
37. Liz-Marzán LM, Giersig M, Mulvaney P. Synthesis of nanosized gold-silica core-shell particles. *Langmuir.* 1996;12:4329-35.
38. Zhao P, Zheng M, Luo Z, et al. NIR-driven smart theranostic nanomedicine for on-demand drug release and synergistic antitumor therapy. *Sci Rep.* 2015;5:14258.
39. Wang B, Yuan H, Liu Z, et al. Cationic oligo(p-phenylene vinylene) materials for combating drug resistance of cancer cells by light manipulation. *Adv Mater.* 2014;26:5986-90.
40. Bonnett R, Martinez G. Photobleaching of sensitizers used in photodynamic therapy. *Tetrahedron.* 2001;57:9513-47.
41. Vernier PT, Levine ZA, Wu YH, et al. Electroporating fields target oxidatively damaged areas in the cell membrane. *PLoS one.* 2009;4:e7966.
42. Su J, Sun H, Meng Q, et al. Long circulation red-blood-cell-mimetic nanoparticles with peptide-enhanced tumor penetration for simultaneously inhibiting growth and lung metastasis of breast cancer. *Adv Funct Mater.* 2016;26:1243-52.
43. Wu M, Meng Q, Chen Y, et al. Large-pore ultrasmall mesoporous organosilica nanoparticles: micelle/precursor co-templating assembly and nuclear-targeted gene delivery. *Adv Mater.* 2015;27:215-22.
44. Slowing II, Wu CW, Vivero-Escoto JL, et al. Mesoporous silica nanoparticles for reducing hemolytic activity towards mammalian red blood cells. *Small.* 2009;5:57-62.
45. Walski T, Dyrda A, Dzik M, et al. Near infrared light induces post-translational modifications of human red blood cell proteins. *Photochem Photobiol Sci.* 2015;14:2035-45.
46. Mi XQ, Chen JY, Cen Y, et al. A comparative study of 632.8 and 532 nm laser irradiation on some rheological factors in human blood in vitro. *J Photochem Photobiol B.* 2004;74:7-12.
47. Kujawa J, Pasternak K, Zawodnik I, et al. The effect of near-infrared MLS laser radiation on cell membrane structure and radical generation. *Lasers Med Sci.* 2014;29:1663-8.
48. Su J, Sun H, Meng Q, et al. Bioinspired nanoparticles with nir-controlled drug release for synergistic chemophotothermal therapy of metastatic breast cancer. *Adv Funct Mater.* 2016. doi:10.1002/adfm.201603381.